Electronic Supplementary Information

Single-atom Tungsten Doping Induced Chemical-electrochemical Coupled Pathway on $Ni(OH)_2$ Enables Efficient Urea Electrooxidation

Lebin Cai[1#], Haoyun Bai[2#], Jilong Li[1#], Feng Xie[1], Kang Jiang[1], Ying-Rui Lu[3], Hui Pan[2], Yongwen Tan[1*]

[1]*College of Materials Science and Engineering, State Key Laboratory of Advanced Design and Manufacturing Technology for Vehicle Body, Hunan University, Changsha, Hunan 410082, China*

[2]*Institute of Applied Physics and Materials Engineering, University of Macau, Macao S. A. R., China*

[3]*National Synchrotron Radiation Research Center, Hsinchu, 300092, Taiwan*

[#] *Lebin Cai, Haoyun Bai and Jilong Li contributed equally to this work*

[*] *Correspondence to: tanyw@hnu.edu.cn*

Supplementary note 1. Calculation of the electrochemical surface area (ECSA) and ECSA-normalized LSV.

The ECSA of all catalysts was calculated according to the double-layer capacitance (C_{dl}) by the CV method.

$$A_{ECSA} = \frac{C_{dl}}{C_s} \times A_{Geo}$$

Therefore, the ECSA-normalized LSV was obtained according to the following formula:

$$j_{ECSA} = j_{Geo} \times \frac{C_{dl}}{C_s}$$

In 1 M KOH electrolyte, a C_s value of 0.05 mF cm^{-2} was chosen for the smooth $Ni(OH)_2$ surface.

Supplementary note 2. XAS measurement and analysis.

The W L_3-edge and Ni K-edge X-ray absorption spectroscopy (XAS) spectra were measured at the beamline BL17C1 and BL01C1 of the National Synchrotron Radiation Research Center, Taiwan. Considering the low loading of W atoms, the W L_3-edge data was collected in fluorescent mode. The incident photon energy was calibrated by using standard metal foil. Each XAS data in this work were obtained by merging more than three groups of data to ensure the accuracy of measurement. The X-ray absorption near-edge structure (XANES) and extended X-ray absorption fine structure (EXAFS) data were processed according to standard procedures using the ATHENA module implemented in the IFEFFIT software packages. Considering the effective quality of EXAFS data, the range of *k* was set to 3.0 ~ 11.0 Å^{-1} for the Fourier transform (Hanning

window, Rbkg = 1).

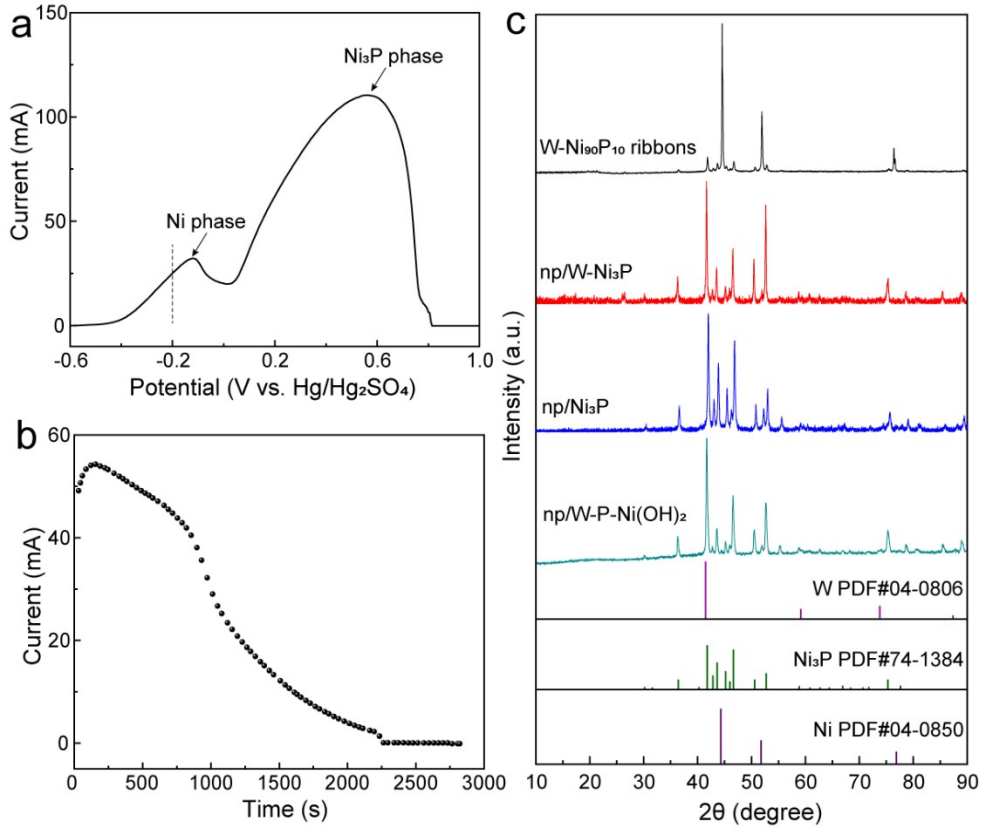

Fig. S1 The fabrication of np/W-Ni_3P. (a) The LSV of W-$Ni_{90}P_{10}$ ribbons in 0.5 M HCl. The potential is calibrated to $Hg/HgSO_4$ reference electrode. The oxidation peaks at ~ -0.2 V and 0.6 V are the corrosion of Ni phase and Ni_3P phase, respectively. A corrosion potential of -0.2 V was chosen to etch the Ni phase and reserve Ni_3P phase; (b) The chronoamperometry of W-$Ni_{90}P_{10}$ ribbons at an applied potential of -0.2 V vs. $Hg/HgSO_4$ in 0.5 M HCl. The zero value of corrosion current represents the complete etching of Ni phase. (c) The XRD pattern of original W-$Ni_{90}P_{10}$ ribbons, np/W-Ni_3P, np/Ni_3P and np/W-P-$Ni(OH)_2$. The standard crystal structures of Ni_3P (PDF#74-1384), Ni (PDF#04-0850) and W (PDF#04-0806) is given as comparison.

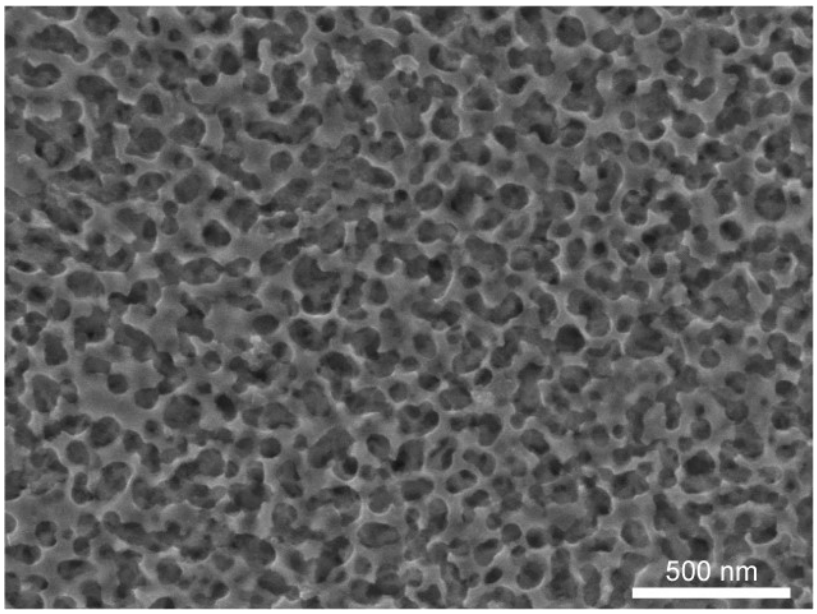

Fig. S2 The SEM of of np/W-P-Ni(OH)$_2$. The self-supported nanoporous structure enables fast gas/liquid mass transfer across the electrode.

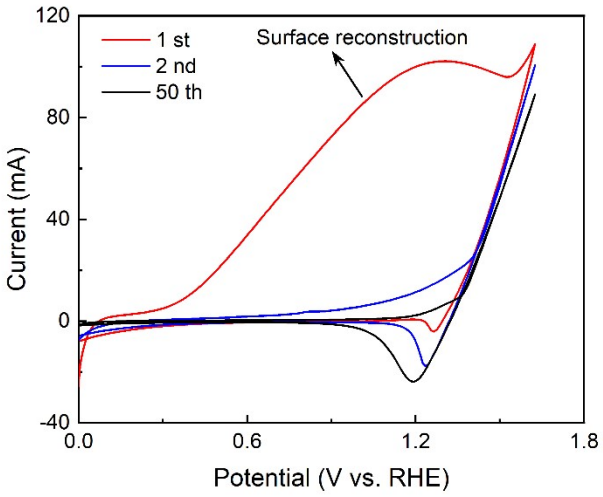

Fig. S3 The 50 cycles in CV activation of np/W-P-Ni_3P electrode. It can be observed that the surface reconstruction is quickly finished during the first CV circle with increasing oxidation current.

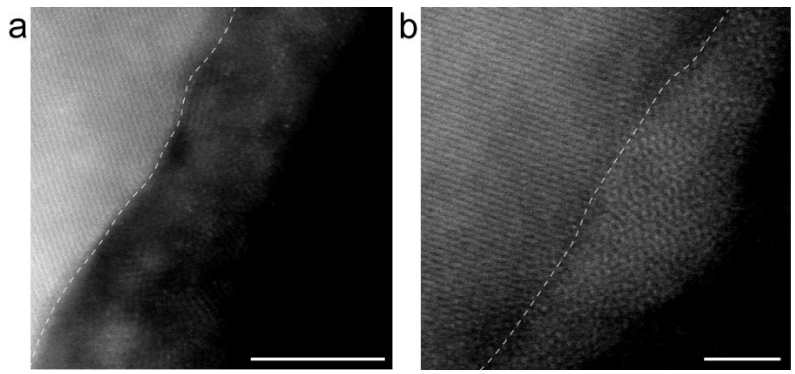

Fig. S4 The HAADF-STEM images of np/W-P-Ni(OH)$_2$ electrode. Scale bar: (a) 5nm; (b) 2nm.

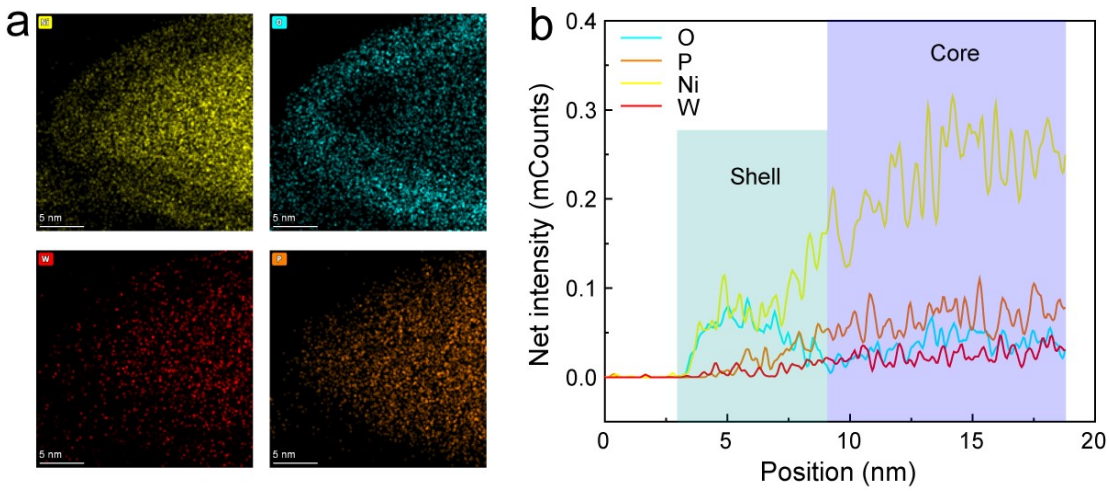

Fig. S5 The EDS of in-situ reconstructed core-shell structure of np/W-P-Ni(OH)$_2$. (a) The EDS mapping of each element in np/W-P-Ni(OH)$_2$. (b) The line-scanning intensity profile along with the radial direction in Figure 1d.

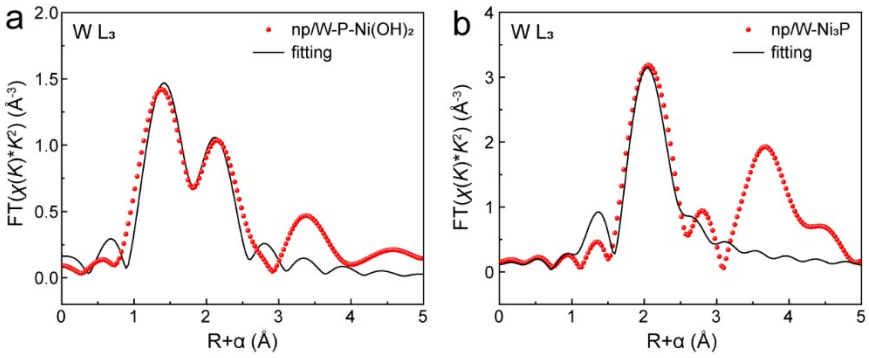

Fig. S6 The fitting W-L_3 edge FT-EXAFS of np/W-P-Ni$(OH)_2$ and np/W-Ni_3P. The fitting parameters is listed in Tab. S2. The strong W-O scattering with coordination number of 4.5 evidences the exist of W single atoms in Ni$(OH)_2$ shell. Note that the coordination of W single atoms is nearly saturated, indicating that atomic W is tend to locate in the subsurface of Ni$(OH)_2$.

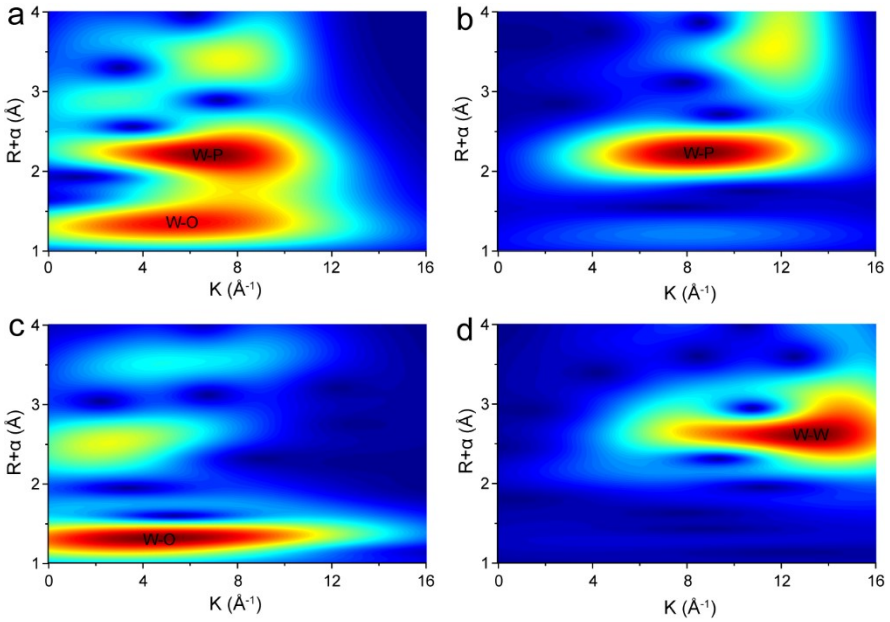

Fig. S7 The WT-EXAFS of (a) np/W-P-Ni(OH)$_2$; (b) np/W-Ni$_3$P; (c) WO$_3$; (d) W foil.

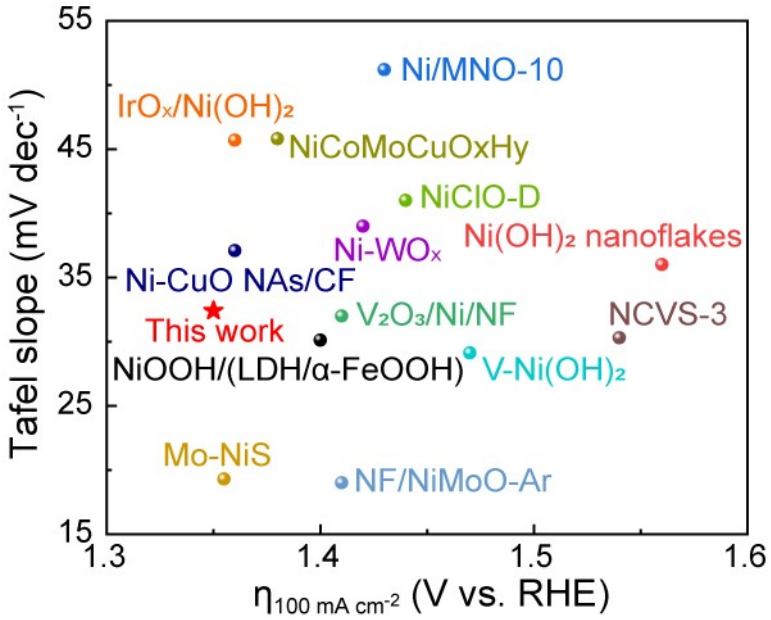

Fig. S8 The comparison of the UOR performance between this work and state-of-art catalysts. The Tafel slope and overpotential data is obtained from different nickel-based catalysts that have been reported. The specific data are listed in **Supplementary Tab. 1.**

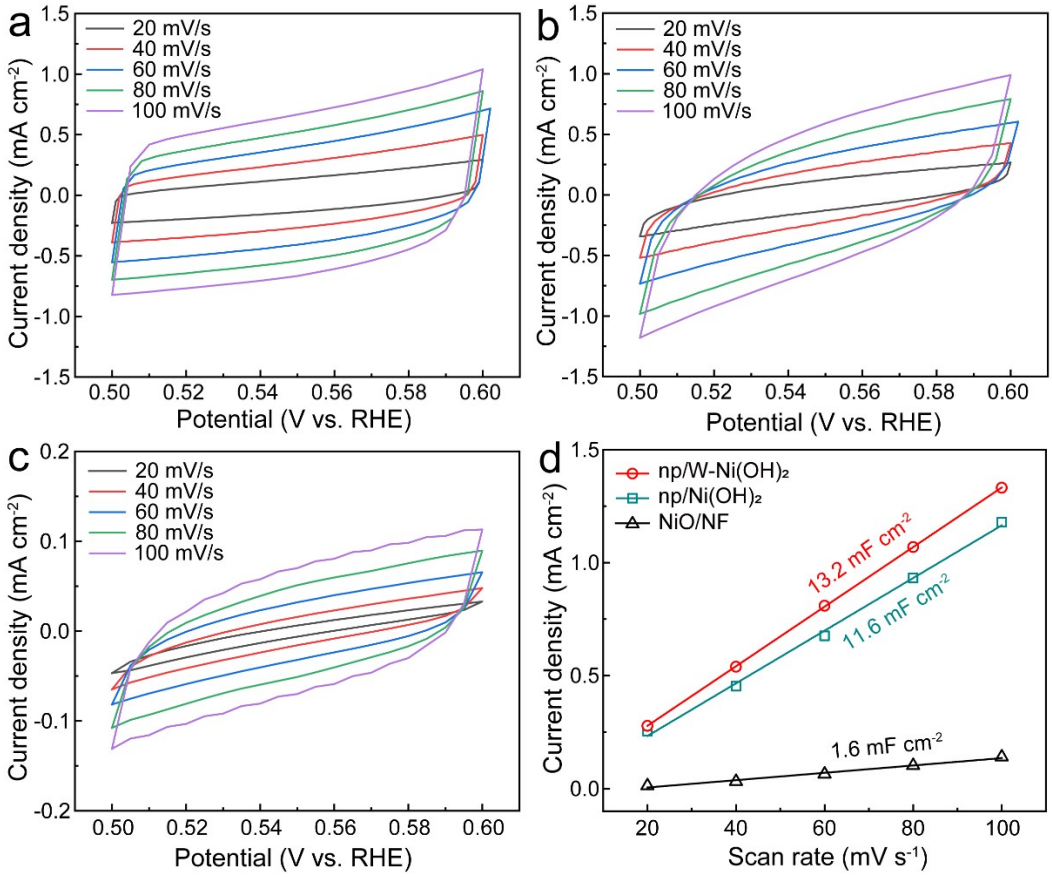

Fig. S9 The quantification of electrochemical active surface area (ECSA) of all catalysts. The CV curves of (a) np/W-P-Ni(OH)$_2$; (b) np/P-Ni(OH)$_2$; (c) NiO/NF. The double layer capacity (C_{dl}) was measured by the CV method. The CV curves were obtained in a non-Faraday potential range of 0.5-0.6 V vs. RHE with different scan rate of 20; 40; 60; 80; 100 mV/s. (d) The fitting curves of double layer current versus scan rate. The slope value of the fitting curves represents the C_{dl} value of catalysts.

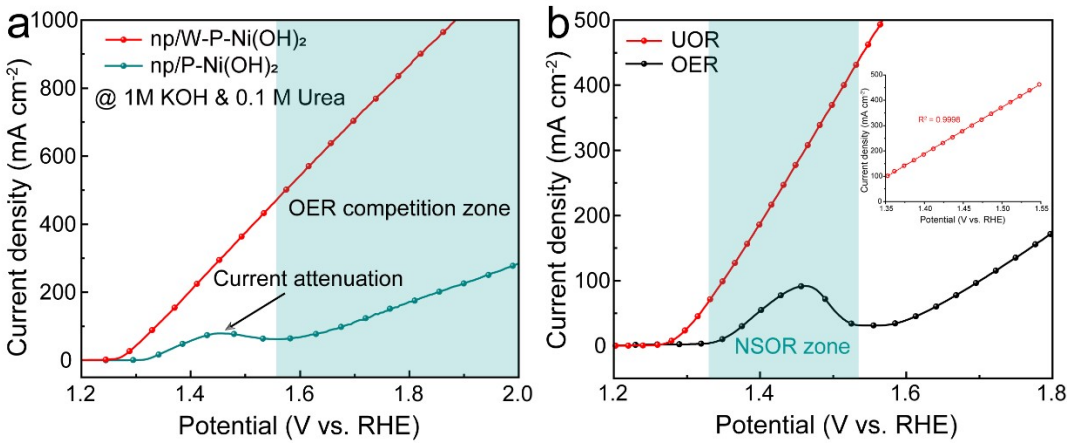

Fig. S10 The LSV curves of np/W-P-Ni(OH)$_2$ and np/P-Ni(OH)$_2$. (a) The LSV curves of np/W-P-Ni(OH)$_2$ and np/P-Ni(OH)$_2$ in 1 M KOH with 0.1 M urea. The current attenuation in the LSV curve of np/P-Ni(OH)$_2$ represents the formation of NiOOH, leading to the competition OER. (b) The LSV curves of np/W-P-Ni(OH)$_2$ for UOR and OER. The inset is the fitting curve of the data points obtained from the UOR LSV in NSOR zone. There is an obvious anode peak at 1.46 V in the LSV of np/P-Ni(OH)$_2$, which is attributed to the current attenuation induced by the competition of OER. However, np/W-P-Ni(OH)$_2$ shows a linear relationship without the current attenuation, indicating W doping enhances the selectivity towards UOR.

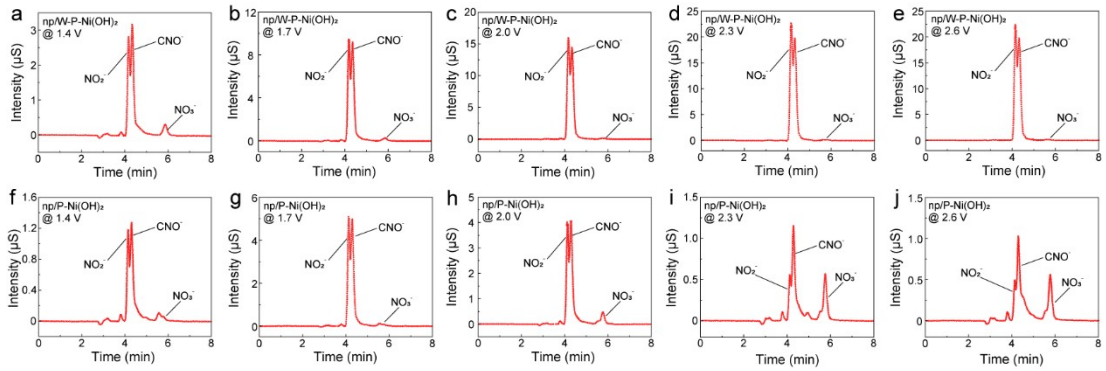

Figure S11. The data of ion chromatography measurements for np/W-P-Ni(OH)$_2$ and np/P-Ni(OH)$_2$ at different potentials. The concentration of CNO^- in electrolyte is comparable with NO_2^- concentration. Therefore, it can be concluded that CNO^- is the final product but not reaction intermediate.

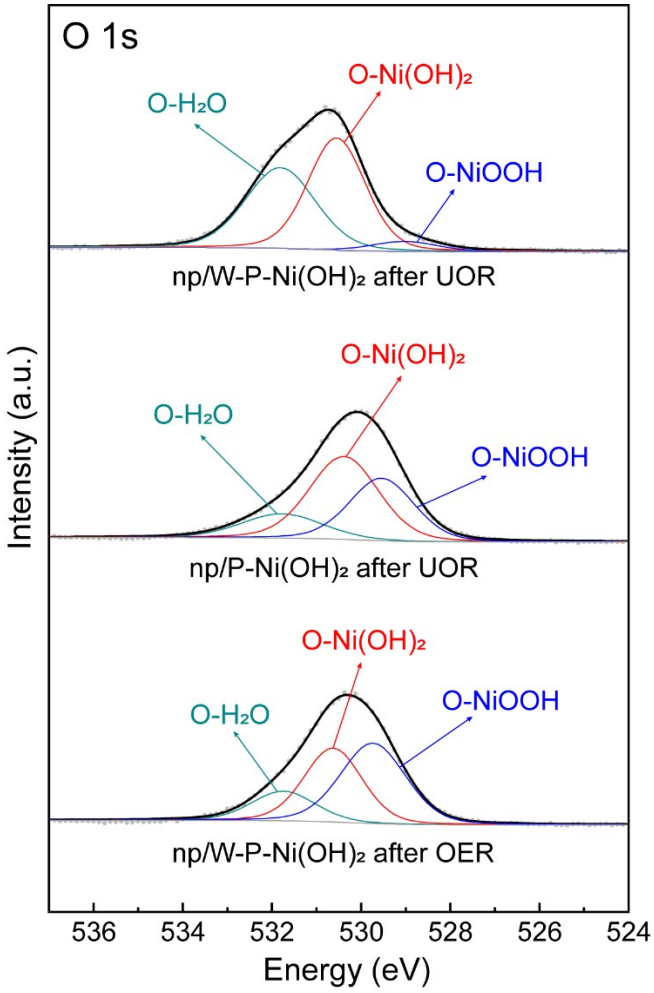

Fig. S12 The O 1*s* XPS of np/W-P-Ni(OH)$_2$ and np/P-Ni(OH)$_2$ after reaction. The O 1s spectra is splitting to three peaks of O-NiOOH, O-Ni(OH)$_2$, and O-H$_2$O. The integral area of O-NiOOH represents the accumulated Ni(OH)O to form NiOOH during reaction. The integral area of O-Ni(OH)$_2$ represents the Ni(OH)$_2$-Ni(OH)O circulation during reaction.

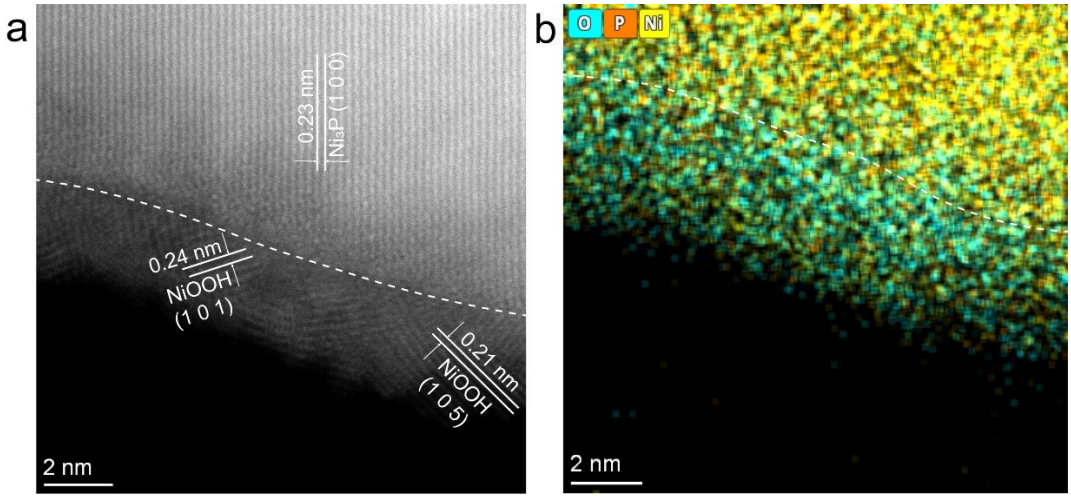

Fig. S13 The HAADF-STEM images of np/P-Ni(OH)$_2$ after UOR. (a) The HAADF-STEM image of core-shell structure. The core is the lattice of Ni_3P (1 0 0) facet. The shell is the (1 0 1) and (1 0 5) facet of NiOOH, representing the accumulation of Ni(OH)O due to the sluggish UOR on np/P-Ni(OH)$_2$ electrode. (b) The EDS mapping of superimposed elements.

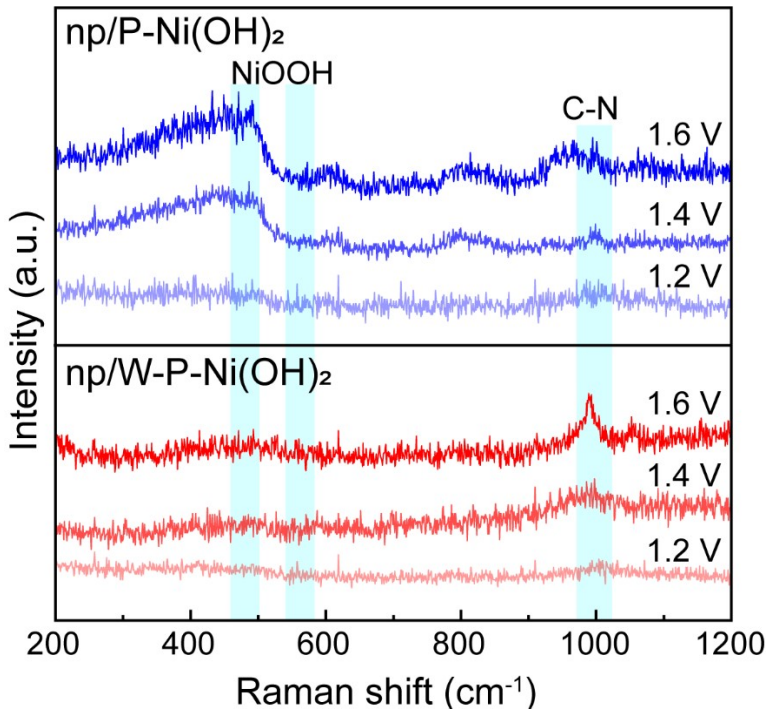

Fig. S14 The in-situ Raman spectra of np/W-P-Ni(OH)$_2$ and np/P-Ni(OH)$_2$ during UOR. The in-situ Raman spectra was obtained in 1 M KOH with 0.33 M urea by using a 532 nm laser. The data at 1.2 V, 1.4 V, and 1.6 V was chosen to make a comparison to demonstrate the role of W in stabilizing the surface active species.

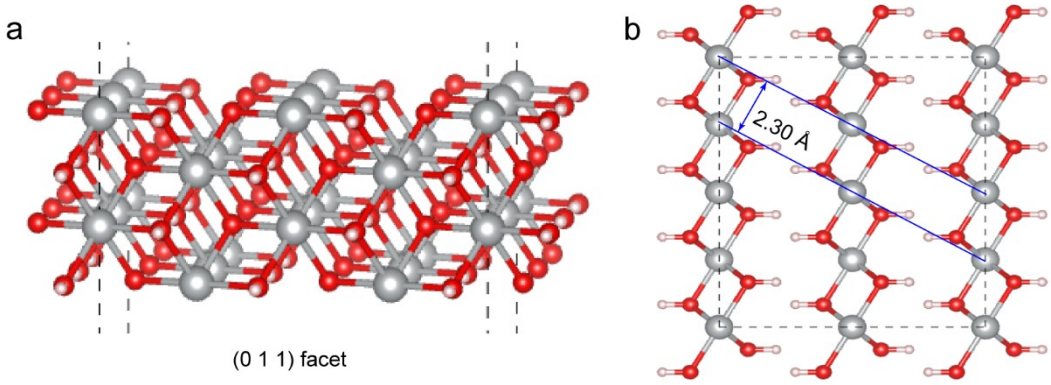

Fig. S15 The theoretical model of pure $Ni(OH)_2$. (a) The (0 1 1) facet of pure $Ni(OH)_2$. (b) The optimized $Ni(OH)_2$ model. The lattice distance is 2.30 Å, correlated with the HAADF-STEM results. It can be seen that both Ni and O atoms are on the surface layer, which is reasonable for the chemical-electrochemical coupled UOR. Gray atom: Ni; red atom: O; pink atom: H.

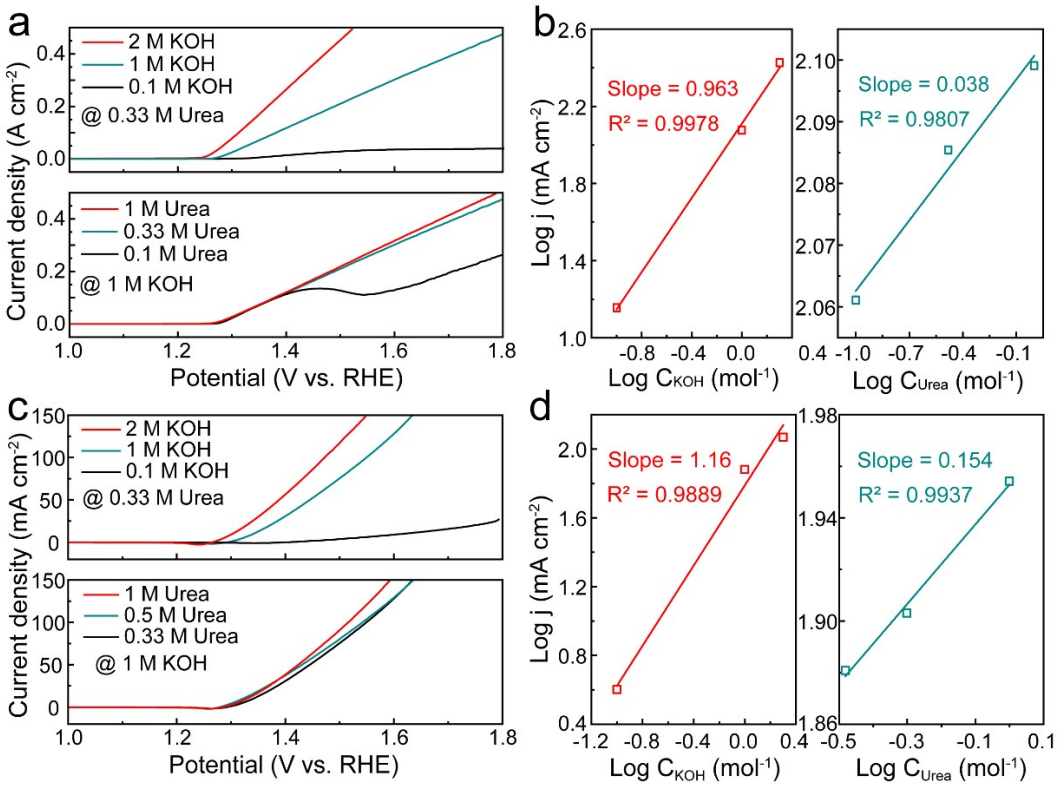

Fig. S16 The electrochemical kinetics analysis of np/P-Ni(OH)$_2$ and Ni(OH)$_2$/NF. (a) The LSV curves of np/P-Ni(OH)$_2$ in different concentrations of KOH and urea. (b) The fitting curves according to the current density and concentrations from (a) at 1.4 V. The slope value represents the reaction order, which demonstrates the dependence of the reaction rate on the concentration of the reactants. (c) The LSV curves of Ni(OH)$_2$ in different concentrations of KOH and urea. (d) The fitting curves according to the current density and concentrations from (a) at 1.5 V.

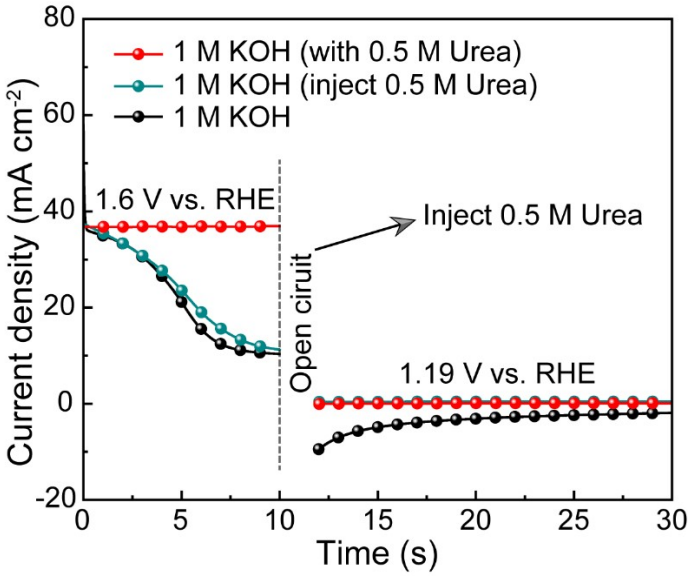

Fig. S17 The multiple-potential step curves of np/P-Ni(OH)$_2$. First, a high oxidation potential of 1.6 V vs. RHE was set for np/P-Ni(OH)$_2$ electrode to enrich the Ni(OH)O species. Then, 0.5 M urea was injected during the open circuit state of 2 s to make Ni(OH)O react with urea adequately. Finally, the potential was switched to 1.19 V (the open circuit potential) to identify the residual Ni(OH)O species.

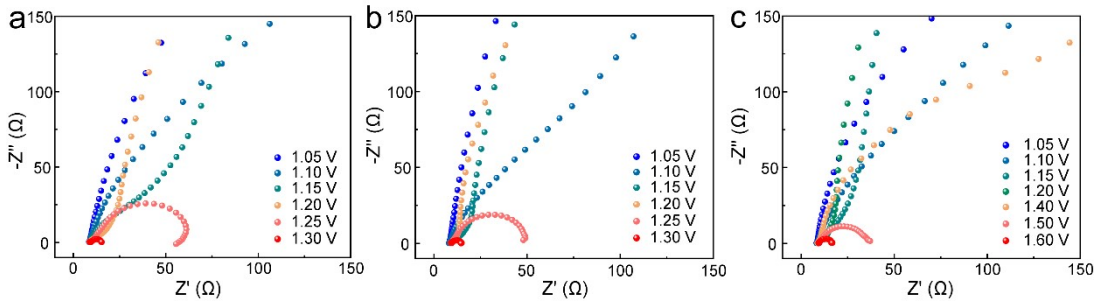

Fig. S18 The in-situ EIS Nyquist plots of np/W-P-Ni(OH)$_2$ and np/P-Ni(OH)$_2$. (a) The in-situ EIS Nyquist plots of np/W-P-Ni(OH)$_2$ for UOR from 1.05 V to 1.3 V. (b) The in-situ EIS Nyquist plots of np/P-Ni(OH)$_2$ for UOR from 1.05 V to 1.3 V. (c) The in-situ EIS Nyquist plots of np/W-P-Ni(OH)$_2$ for OER from 1.05 V to 1.6 V.

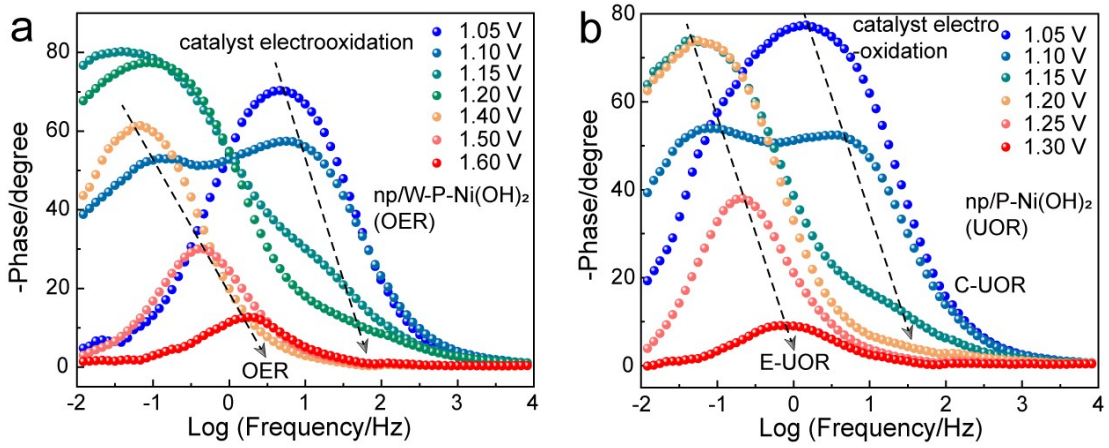

Fig. S19 The in-situ EIS Bode plots of (a) np/W-P-Ni(OH)$_2$ for OER and (b) np/P-Ni(OH)$_2$ for UOR. (a) The data was collected at a frequency range of 10000~0.01 Hz from 1.05 V to 1.6 V. The middle frequency includes the electrooxidation of np/W-P-Ni(OH)$_2$ and the low frequency represents the electrochemical oxygen oxidation on the np/W-P-Ni(OH)$_2$ electrode. (b) The data was collected at a frequency range of 10000~0.01 Hz from 1.05 V to 1.3 V. The middle frequency includes the electrooxidation of np/P-Ni(OH)$_2$ and the spontaneously chemical dehydrogenation of urea. The low frequency represents the electrochemical urea oxidation on the oxidated np/P-Ni(OH)$_2$ electrode.

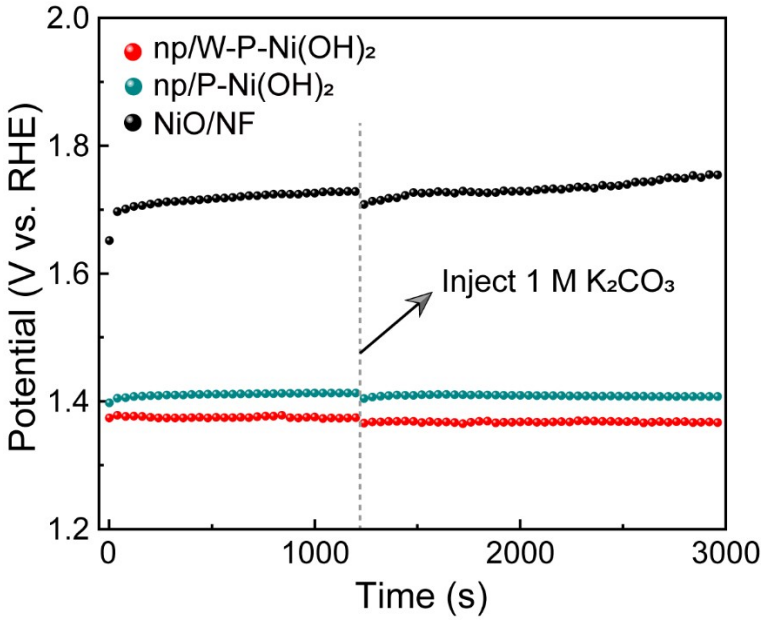

Fig. S20 The chronopotentiometry curves of np/W-P-Ni(OH)$_2$, np/P-Ni(OH)$_2$, and NiO/NF. The chronopotentiometry curves were obtained at 50 mA cm^{-2} in 1 M KOH with 0.5 M urea. After 1200 s, 2 ml 1 M K_2CO_3 solution was injected into the electrolyte. When 2 ml 1 M K_2CO_3 solution was injected into the electrolyte, NiO/NF showed obvious activity decay, which can be attributed to the too-strong adsorption of *COO on the NiOOH surface. However, there are no clear changes on np/W-P-Ni(OH)$_2$ and np/P-Ni(OH)$_2$ electrodes, evidencing that the desorption of *COO is not limited on Ni(OH)O. This also correlates with the vibration of CO_3^{2-} located at 1396 cm^{-2} on np/W-P-Ni(OH)$_2$ electrode in the in-situ SEFT-IR.

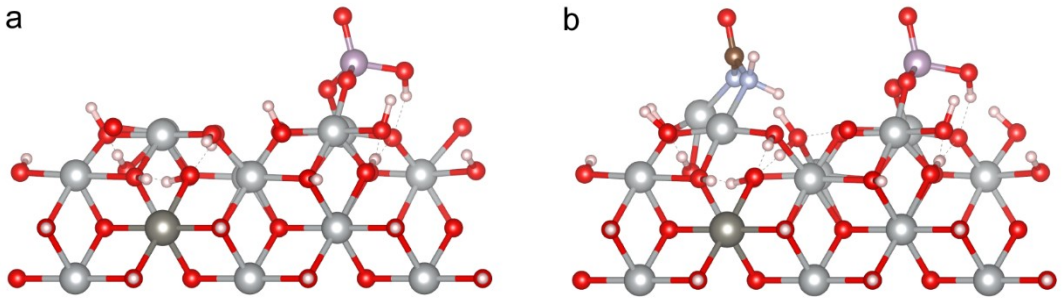

Fig. S21 The theoretical model of W-P-Ni(OH)$_2$ before and after adsorbing urea molecule. Gray atom: Ni; dark atom: W; red atom: O; pink atom: H; blue atom: N; brown atom: C; purple atom: P.

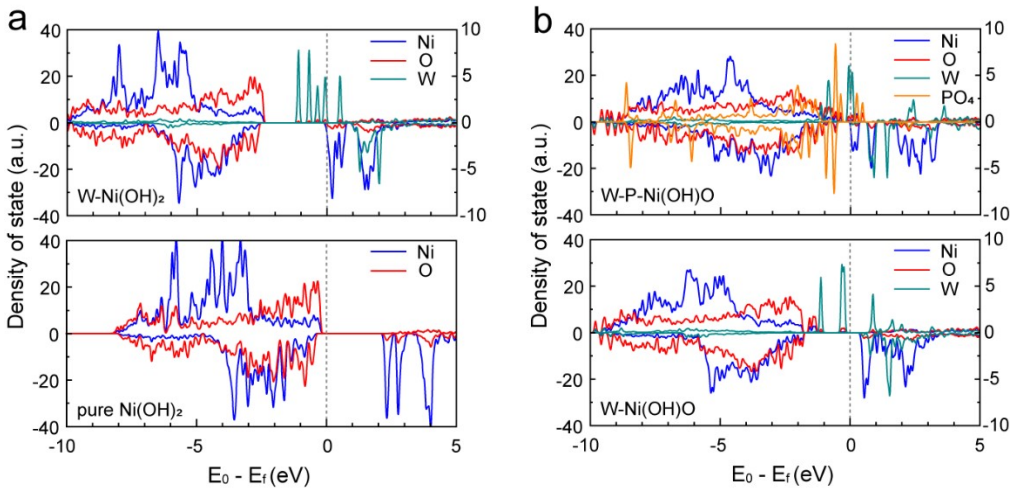

Fig. S22 The comparison between the DOS of different structures. (a) The DOS of W-Ni$(OH)_2$ and pure Ni$(OH)_2$. (b) The DOS of W-P-Ni(OH)O and W-Ni(OH)O. Obviously, W doping induces a strongly localized state, correlated with the Bader analysis result. Electron localization means the transition of Ni atoms from a metallic state to a semi-metallic state, which is not conducive to the six-electron-transfer urea electrooxidation. However, after adsorbing PO_4^{2-}, the energy band becomes more complicated and occupies the Fermi level. This result indicates that PO_4^{2-} strengthens the metallic state of Ni sites.

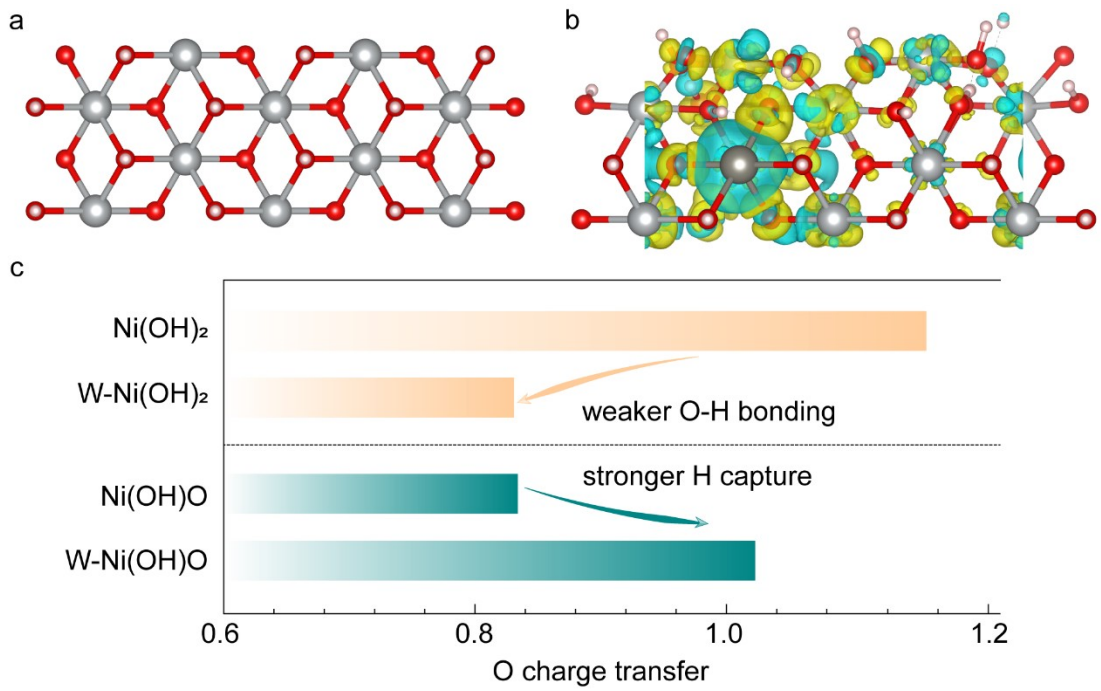

Fig. S23 The Bader analysis of W-doped $Ni(OH)_2$. (a) The (011) facet of pure $Ni(OH)_2$. (b) The charge transfer after W doping. (c) The O charge transfer on different catalyst models. W doped $Ni(OH)_2$ system possesses less charge (6.831) accumulating on the O atom than that of pure $Ni(OH)_2$ (7.159), indicating that the atomic W doping leads to a more positive valence of the O atom, that is to say, the O-H bonding is weakened so that the hydroxyl dehydrogenation process can be more likely to happen. Interestingly, when H vacancy forms, O gets less charge in pure $Ni(OH)_2$ surface, but gets more charge in W doped system. This difference demonstrates that W has strong electron regulations on O sites. Therefore, O sites with more charge accumulated have a stronger tendency to spontaneously bind the H atoms in urea molecular, thus facilitating the chemical UOR process. The yellow area represents the accumulation of the bader charge, and the blue area represents the loss of the bader charge. Gray atom: Ni; dark atom: W; red atom: O; pink atom: H.

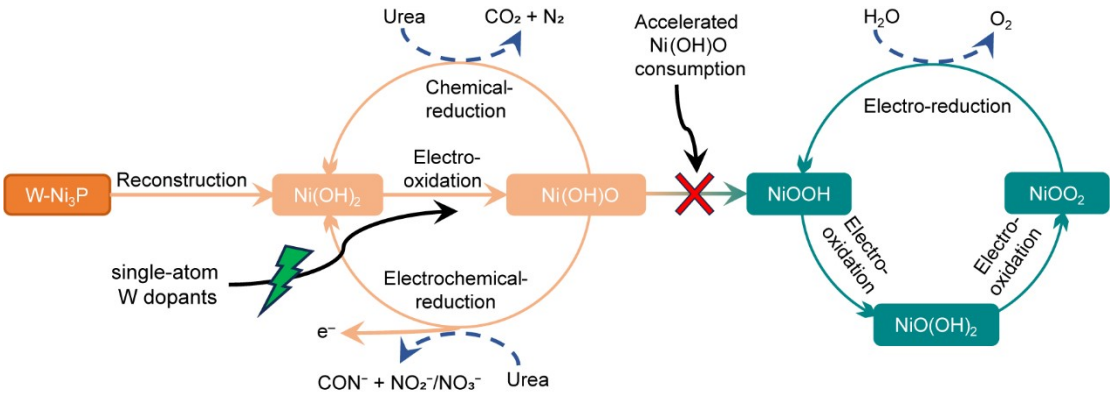

Fig. S24 The competition mechanism on np/W-P-Ni(OH)$_2$ electrode. The W doping realizes the virtuous circle between Ni(OH)$_2$ and Ni(OH)O by simultaneously accelerating the generation and consumption of Ni(OH)O active species, which can effectively prevent the accumulation of Ni(OH)O to form OER-favored NiOOH species.

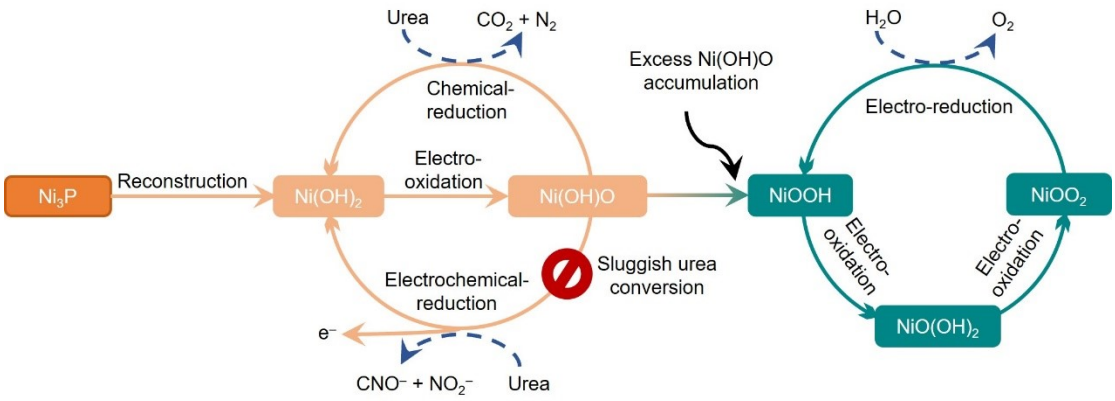

Fig. S25 The competition mechanism on np/P-Ni(OH)$_2$ electrode. The sluggish UOR prevents the Ni(OH)O species from being consumed in time, leading to the accumulation of excess Ni(OH)O to form NiOOH. This active NiOOH can gradually switch the reaction from UOR to OER.

Tab. S1 The element contents of np/W-P-Ni(OH)$_2$ obtained by XPS.

Element	Atomic ratio (at.%)	Mass ratio (wt.%)
Ni	21.99	48.26
O	73.07	43.72
P	4.55	5.27
W	0.40	2.75

Table S2. The fitting parameters of np/W-P-$Ni(OH)_2$ and np/W-Ni_3P.

Samples	Paths	R (Å)	N	ΔE_0 (eV)	σ^2 (Å^2)	R-factor
np/W-P-$Ni(OH)_2$	W-O	1.824	4.5	7.133	0.005	0.031
	W-P	2.471	3.69		0.005	
np/W-Ni_3P	W-P	2.416	2.93	3.009	0.004	0.057

Tab. S3 The UOR performance of this work and other state-of-art nickel-based catalysts.

Catalysts	η@100 mA cm^{-2} (V)	Tafel slope ($mV\ dec^{-1}$)	Electrolyte	Ref
This work	1.35	32.4	1 M KOH & 0.33 M urea	/
NCVS-3	1.54	30.3	1 M KOH & 0.33 M urea	1
V-$Ni(OH)_2$	1.47	29.1	1 M KOH & 0.33 M urea	2
Mo-NiS	1.36	19.3	1 M KOH & 0.5 M urea	3
NiOOH/(LDH/α-FeOOH)	1.40	30.1	1 M KOH & 0.33 M urea	4
Ni-CuO NAs/CF	1.36	37.1	1 M KOH & 0.33 M urea	5
$Ni(OH)_2$ nanoflakes	1.56	36.0	1 M KOH & 0.33 M urea	6
NF/NiMoO-Ar	1.41	19.0	1 M KOH & 0.5 M urea	7
$IrO_x/Ni(OH)_2$	1.36	45.7	1 M KOH & 0.33 M urea	8

$NiCoMoCuO_xH_y$	1.38	45.8	1 M KOH & 0.33 M urea	9
V_2O_3/Ni/NF	1.41	32.0	1 M KOH & 0.5 M urea	10
Ni/MNO-10	1.43	51.2	1 M KOH & 0.5 M urea	11
NiClO-D	1.44	41.0	1 M KOH & 0.33 M urea	12
Ni-WO_x	1.42	39.0	1 M KOH & 0.33 M urea	13

1

2

Tab. S4 The calculated formation energy (E_f) of the hydroxyl dehydrogenation process on pure $Ni(OH)_2$ and W doped $Ni(OH)_2$.

Structures	E_0 before	E_0 after	E_f
$Ni(OH)_2$	-399.488	-393.761	2.31885
W-NiOOH(Ni1)	-405.766	-402.304	0.05288
W-NiOOH(Ni2)		-401.820	0.53691

Tab. S5 The calculated bader charge analysis of pure $Ni(OH)_2$ and W doped $Ni(OH)_2$.

Structures	Charge			
	E_0	Ni	O	W
$Ni(OH)_2$	-398.703	8.761	7.159	
NiOOH	-393.761	8.725	6.834	
W-$Ni(OH)_2$	-405.496	8.785	6.831	12.304
W-NiOOH(Ni1)	-402.304	8.865	7.013	12.865
W-NiOOH(Ni2)	-401.820	8.823	7.023	12.074
	Delta charge			
	Ni	O	W	
$Ni(OH)_2$	-1.239	1.159		
NiOOH	-1.275	0.834		
W-$Ni(OH)_2$	-1.215	0.831	-1.696	
W-NiOOH(Ni1)	-1.135	1.013	-1.135	
W-NiOOH(Ni2)	-1.177	1.023	-1.926	

References

1. Z. Ji, Y. Song, S. Zhao, Y. Li, J. Liu and W. Hu, *ACS Catal.*, 2022, **12**, 569-579.
2. H. Qin, Y. Ye, J. Li, W. Jia, S. Zheng, X. Cao, G. Lin and L. Jiao, *Adv. Funct. Mater.*, 2023, **33**, 2209698.
3. Y. Zhou, Y. Wang, D. Kong, Q. Zhao, L. Zhao, J. Zhang, X. Chen, Y. Li, Y. Xu and C. Meng, *Adv. Funct. Mater.*, 2023, **33**, 2210656.
4. M. Cai, Q. Zhu, X. Wang, Z. Shao, L. Yao, H. Zeng, X. Wu, J. Chen, K. Huang and S. Feng, *Adv. Mater.*, 2023, **35**, 2209338.
5. H. Sun, J. Liu, H. Kim, S. Song, L. Fei, Z. Hu, H. J. Lin, C. T. Chen, F. Ciucci and W. Jung, *Adv. Sci.*, 2022, **9**, 2204800.
6. W. Yang, X. Yang, C. Hou, B. Li, H. Gao, J. Lin and X. Luo, *Appl. Catal. B: Environ.*, 2019, **259**, 118020.
7. Z.-Y. Yu, C.-C. Lang, M.-R. Gao, Y. Chen, Q.-Q. Fu, Y. Duan and S.-H. Yu, *Energy & Environ. Sci.*, 2018, **11**, 1890-1897.
8. Q. Zheng, Y. Yan, J. Zhong, S. Yan and Z. Zou, *Energy Environ. Sci.*, 2024, **17**, 748-759.
9. R. Li, Y. Li, P. Yang, P. Ren, D. Wang, X. Lu, H. Zhang, Z. Zhang, P. Yan, J. Zhang, M. An, B. Wang, H. Liu and S. Dou, *Small*, 2023, **19**, 2302151.
10. Q. Zhang, B. Liu, L. Li, Y. Ji, C. Wang, L. Zhang and Z. Su, *Small*, 2021, **17**, 2005769.
11. V. Maheskumar, A. Min, C. J. Moon, R. A. Senthil and M. Y. Choi, *Small Struct.*, 2023, **4**, 2300212.
12. L. Zhang, L. Wang, H. Lin, Y. Liu, J. Ye, Y. Wen, A. Chen, L. Wang, F. Ni, Z.

Zhou, S. Sun, Y. Li, B. Zhang and H. Peng, *Angew. Chem. Int. Ed.*, 2019, **58**, 16820-16825.

13. L. Wang, Y. Zhu, Y. Wen, S. Li, C. Cui, F. Ni, Y. Liu, H. Lin, Y. Li, H. Peng and B. Zhang, *Angew. Chem. Int. Ed.*, 2021, **60**, 10577-10582.